Closed-Loop Shape-Forming Control of a Magnetic Soft Continuum Robot

Vittorio Francescon[1], Nikita Murasovs[1], Peter Lloyd[1],
Onaizah Onaizah[2], Damith Suresh Chathuranga[3], Pietro Valdastri[1]

***Abstract*—Continuum manipulators are frequently employed in endoluminal interventions, however, a lack of softness and dexterity in standard manipulators can risk trauma during navigation and limit reachable workspace. Magnetically actuated Soft Continuum Robots (MSCRs) offer enhanced miniaturization potential and reduced rigidity due to their external actuation. Magnetizations pertaining only to the tip of the robot offer a limited range of deformation options where more versatile MSCRs can be embedded with distinct, lengthwise magnetization profiles. These full-body bespoke profiles allow the robots to form pre-determined shapes under actuation. Here we propose an approach to model and control MSCR behavior in closed-loop. We employ this system to achieve shape forming navigations subject to variations in initial conditions. To validate our methodology, we conduct experiments using a 50 mm long by 1.8 mm diameter MSCR navigating through a soft phantom from the tip of a duodenoscope. The proposed system is capable of rejecting variations in the angle at which the MSCR is inserted. We employed homogeneous magnetic fields for actuation and closed-loop vision-based control to manipulate the lengthwise body shape of our MSCR. The performance of this closed-loop approach is compared with an open loop counterpart, which fails in all but one navigation attempts into the pancreatic duct.**

***Index Terms*—Modeling, Control, and Learning for Soft Robots; Medical Robots and Systems; Magnetic Actuation.**

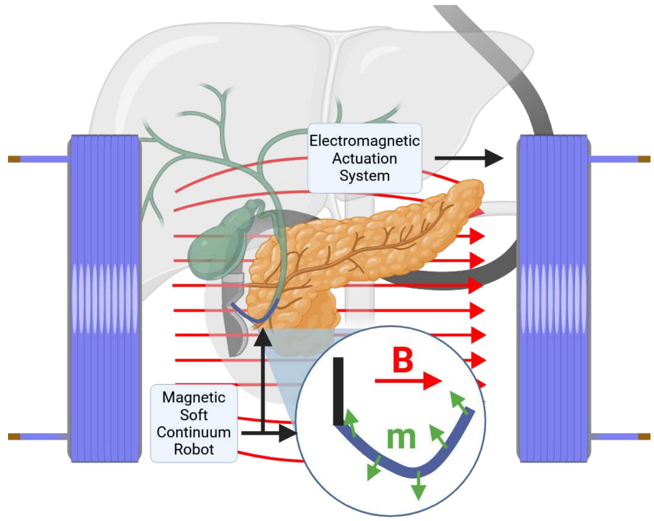

Fig. 1. A magnetically actuated soft-continuum robot employed in an endoluminal operation. The robot is introduced through the instrument channel of a duodenoscope and externally manipulated by an applied magnetic field $\mathbf{B}$ (red arrow). Shape forming is induced by the magnetic torque generated through the interaction of the remnant magnetization ($\mathbf{m}$, green arrows) of the MSCR and the applied field $\mathbf{B}$. Created in BioRender. Francescon, V. (2024) https://BioRender.com/a47v740.

I. INTRODUCTION

CONTINUUM manipulators, in the form of surgical catheters, are widely employed in traditional endoluminal procedures [1]. Here, a thoroughly trained surgeon manually guides the manipulator via a system of cables allowing control of a flexible end-effector where a sensor or tool is attached for surgical procedures. Endoscopic retrograde cholangio pancreatography (ERCP) [2] is one such endoluminal procedure in which an endoscope is inserted through the gastrointestinal tract and guided under fluoroscopy to inspect and potentially operate in the biliary system. Once the endoscopic tools reach the appropriate position in the duodenum, a catheter is deployed through the major duodenal papilla, where it may be directed through the pancreatic duct or in the bile duct. The deployed catheter can be employed to remove tissue or dislodge gallstones. Due to the rigidity introduced by the actuation system and the potential for human error, there exists a concrete risk to the patient of trauma caused from excessive or forceful contact with the internal lumen [3].

Hence, autonomous control of a continuum manipulators' shape is highly desirable. This control can offer valuable support to the surgeon during procedures, reducing manual effort and risk of human error [3]. Additionally, this automation can be utilized to limit the robot's interaction with internal lumen, thereby decreasing the risk of both tissue damage and buckling of the flexible catheter [3]. Further, such an implementation can not only lead to shorter procedure times but also, due to its size, expand the reachable workspace.

While multiple avenues exist regarding the actuation system used for any continuum robots [1], magnetics exhibit extrinsic actuation and hence high miniaturization potential whilst retaining a high degree of shape control. Such Magnetic Soft Continuum Robots (MSCRs) are therefore exploitable for

Manuscript received: October, 31, 2025; Revised March, 03, 2025; Accepted April, 16, 2025. This paper was recommended for publication by Editor J. Burgner-Kahrs upon evaluation of the Associate Editor and Reviewers' comments. This work was supported in part by the Engineering and Physical Sciences Research Council (EPSRC) under Grants EP/R045291/1 and EP/V009818/1, and in part by the European Research Council (ERC) through the European Union's Horizon 2020 Research and Innovation Programme under Grant 818045. *(Corresponding Author: Vittorio Francescon.)*

[1]Vittorio Francescon, Nikita Murasovs, Peter Llyoyd and Pietro Valdastri are with Storm Lab UK, School of Electronic and Electrical Engineering, University of Leeds, LS2 9JT Leeds, U.K. el21vf@leeds.ac.uk; elnmur@leeds.ac.uk; P.Lloyd@leeds.ac.uk; P.Valdastri@leeds.ac.uk

[2]Onaizah Onaizah is with HEART Lab, McMaster University, 1280 Main St. West, Hamilton, ON L8S 4L8 onaizaho@mcmaster.ca

[3]Damith Suresh Chathuranga is with the Department of Mechanical Engineering, University College London, WC1E 7JE London, U.K. d.vithanage@ucl.ac.uk

Digital Object Identifier (DOI): see top of this page.

endoscopic procedures in place of standard catheters, as has been shown in the literature, [1], [4] and in Fig. 1.

Prior works have focused on producing an MSCR to be controlled about its distal end [5]–[7] or *tip*. Controlling the whole length of the robot's body (or *full body shape-forming*) has relevance as a way of minimizing normal contact forces during navigation, as well as shear forces and the friction associated with them. This approach utilizes bespoke magnetization profiles as a programming parameter, empowering the MSCR to undertake more complex pre-defined shapes when actuated [8], [9]. Full-body shape-forming has been demonstrated in the context of tendon-driven continuum robots [10] and is often used in untethered robots [11]. While magnetic actuation allows for extrinsic actuation of an MSCR, it also imposes a limit to the actuating potential of the system. As such, attempting to control an arbitrary number of sections of the robot with the limited actuatable DoF allowed by magnetics renders full-body shape-forming much more challenging than solutions concerned only with the distal end of the catheter. The task is essentially reduced to bind the virtually infinite DoF present in a continuum manipulator to an actuation system capable of a limited number of linearly connected wrenches. Hence, MSCRs can be considered in a state of constant singularity, where an infinite number of configurations are possible for any given desired end-goal. As a result, the solution space for this length-wise magnetized manipulator must be reduced in size via a minimization algorithm. This has been approached through various methods such as least-square solutions [6], [12] or gradient based methods [13].

Both tip-driven and full-body shape-forming approaches necessitate simplifying the behaviour of the MSCRs to facilitate modeling. This need arises from the inherent lack of rigidity commonly associated with Continuum Robots, resulting in a considerably more complex relationship between the actuating system and the robot's end effector compared to classical rigid manipulators. Furthermore, the MSCRs under discussion exhibit hyper-elastic characteristics and potentially intricate geometries, collectively contributing to a significant modeling challenge [4]. Pseudo rigid-link assumptions [14], [15] sacrifice longitudinal behaviour (i.e. compression and extension) exhibited by the soft robot to improve run-time performance. Given reasonably accurate stiffness parameters, pseudo rigid-link assumptions can effectively capture an MSCR under deformation. Issues may however arise when the input parameters cannot accurately be determined. In [16], Da Veiga et al. explore the different materials currently used for MSCRs and locate a principle problem in the non-uniform stiffness of materials such as Ecoflex™ 00-30. Therefore, the material properties of an MSCR are considered here as input parameters to a control model, allowing for adjustments at run-time to best fit the MSCR at a given station as well as compensating for any unmodeled factors or modeling errors.

Here we offer a solution to the challenge of controlling full body shape in closed-loop for under actuated magnetic catheters by leveraging the computational efficiency of pseudo rigid-link assumptions. We reduce the infinite possible solution space through least-mean squares optimization, minimizing the required actuating magnetic field to obtain the desired shape. In particular, we perform an initial parse of the possible solutions with the goal of locating the lowest possible value that provides an acceptable answer. Subsequently we apply this result and adapt our control model to navigate the remaining solution space using real-time visual feedback as a guide.

With this increased degree of control over the robot, we navigate in a follow-the-leader form through a soft phantom and neutralize both external (in the form of variable angle and position of entry) and internal (due to the fabrication process, hyper-elasticity and other unmodeled influences) uncertainties as well as decreasing mechanical resistance due to contact forces [8], [17].

The validity of our approach is demonstrated on a soft phantom representing the major duodenal papilla and the bifurcation to the pancreatic and bile duct. The focus is chiefly placed on the pancreatic duct due to its softness and sensitivity [3] and the risk of trauma caused to the patient during operation [2], [18]. We demonstrate the ability to control the entire body length of a bespoke magnetized catheter. Furthermore, we present a controller that responds to spatial errors at multiple points along the length of the catheter. This allows autonomous follow-the-leader motion without potentially harmful interactive contact forces. The performance of this approach is then proven by repeating the same experiments without implementing the proposed controller, failing to reach the target location.

II. MAGNETICS AND RIGID LINK ASSUMPTIONS

The following section offers a brief overview of magnetic actuation and the pseudo rigid-link representation of continuum robots, as previously presented in [19].

Considering an MSCR under the planar pseudo rigid-link assumption featuring a single link, the robot is assumed to experience actuation solely about its pseudo joint. It follows that any one link can be approximated to a magnetic dipole $\mathbf{m} \in \mathbb{R}^3$. As such, when a magnetic field $\mathbf{B} \in \mathbb{R}^3$ is applied, the resultant torque $\boldsymbol{\tau} \in \mathbb{R}^3$ is given by [20]:

$$\boldsymbol{\tau} = \mathbf{m} \times \mathbf{B} = \mathbf{m}_{\times}\, \mathbf{B} \tag{1}$$

where $[.]_{\times}$ represents the *skew* operator, mapping a $\mathbb{R}^3$ vector into a $\mathbb{R}^{3\times3}$ skew-symmetric matrix and allowing a cross product to be rewritten as matrix multiplication. The torque obtained here will in turn cause an angular displacement between the referential and deformed position of the pseudo joint $\mathbf{q} \in \mathbb{R}^3$. To ensure equilibrium in the system, the magnetically generated torque upon the MSCR will be reflected in mechanical torque, which can be described as:

$$\boldsymbol{\tau} = \mathbf{K}\mathbf{q} = \mathbf{m}_{\times} \cdot \mathbf{B} \tag{2}$$

where, assuming linearly elastic behavior:

$$\mathbf{K} \in \mathbb{R}^{3\times3} = diag(E_x I_x, E_y I_y, GJ)/L \tag{3}$$

where E representing the Young's Modulus of the MSCR, I the section's moment of inertia in each direction, G represents the shear modulus of the MSCR, J represents the sections' polar moment of inertia and L represents the length of the link in question [21]. Expanding the MSCR to now feature n

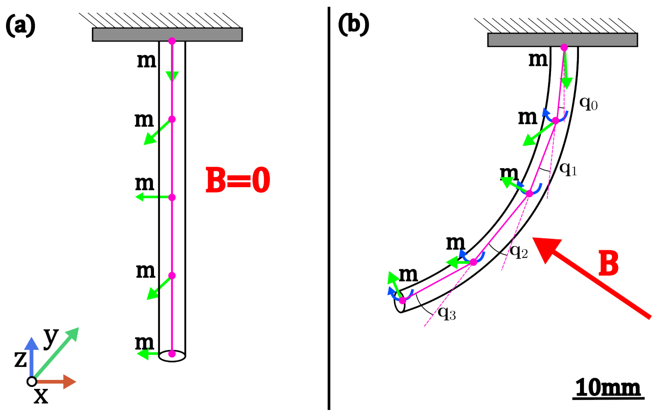

Fig. 2. (a) Planar diagram of an MSCR at rest ($\mathbf{B} = 0$), subdivided into 4 pseudo rigid-links, each with a distinct magnetization of magnitude $|\mathbf{m}|$, with direction indicated by green arrows. The pseudo rigid-link representation of the MSCR is portrayed in purple. (b) Planar view of the MSCR now actuated by field of magnitude $|\mathbf{B}|$ and direction as shown by the respective red arrow, with magnetizations $\mathbf{m}$. The 4 pseudo rigid-link representation is provided in purple and also features the individual angular deflection for each link $\mathbf{q}_i$, measured as phase between the vector aligned with the current link and the vector aligned with the previous link in the chain. The induced torque at each pseudo joint is represented by blue circular arrows.

pseudo spherical joints, (as shown in Fig. 2(b), each pseudo joint will respond to an applied field $\mathbf{B}$ following Equation 1. In the case of this letter, only planar motion is considered. As such, each pseudo joint $\mathbf{q}_i$ possesses a single non-zero component, representing deflection in the plane of bending. Clearly, for a homogeneous field, $\mathbf{B}$ is equal for all links, creating the actuation constraint alluded to in the introduction. Thus, all the resulting joint deflections $\mathbf{q}$ can be stacked into:

$$\mathbf{Q} \in \mathbb{R}^{3\times n} = \begin{bmatrix} \mathbf{q}_0 & \cdots & \mathbf{q}_i & \cdots & \mathbf{q}_{n-1} \end{bmatrix}^T \tag{4}$$

where $\mathbf{q}_i$ represents the deflection at pseudo joint i.

Similarly, the magnetization of each dipole-like link can be vertically stacked:

$$\mathbf{S} = \begin{bmatrix} 0_{3\times3} & \mathbf{m}_{\times_0} & \cdots & 0_{3\times3} & \mathbf{m}_{\times_i} & \cdots & 0_{3\times3} & \mathbf{m}_{\times_n} \end{bmatrix}^T \tag{5}$$

with the $0_{3\times3}$ terms being present for generality but zeroed to account for the lack of magnetic gradients applied here [22]. Magnetic gradients have been removed as an actuation variable due to their relatively small effect on the output torque on the system when compared to the uniform fields applied [23] . In a Helmholtz coil setup, the effect of gradient-based actuation can be considered to be negligible [24]. To refactor Equation 2 for usage in an n-pseudo joint scenario, however, it is important to account for the contribution to each pseudo joint's behavior to the succeeding joints in the chain. To this end, a Jacobian transpose derived from the MSCR's differential kinematics is employed [8].

Thus, a complete expression can be written as:

$$\mathbf{KQ} = \mathbf{J}^T\mathbf{SB} \tag{6}$$

where the n-link version of $\mathbf{K}$ is obtained by repeating Equation 3 n times and $\mathbf{J}^T$ is the transpose of the differential kinematic Jacobian, $\mathbf{J}^T \in \mathbb{R}^{3n\times6n}$.

It is worth noting here that an exact version of Equation 6 would also include the effect of gravity on each individual link. Given the experimental setup, detailed in Section IV, being horizontal and generally low friction, the effect of gravity in this work is considered to be negligible.

III. CONTROLLER

A. Initial Solution

Any given desired shape can be reduced to n sets of three-dimensional angular deflections $\mathbf{Q}_d$, rotations between sequential pseudo rigid-links. Thus, utilizing Equation 6, it is possible to calculate the required field $\mathbf{B}_d$. In this case, it may be tempting to invert the Jacobian term to arrive at a direct analytical solution. Issues arise, however, due to the nature of the Jacobian Matrix involved. These issues stem from the disparity between the actuatable DoF used (3×1 magnetic torque) and the DoF of the robot model ($3 \times n$). Thus, the Jacobian employed is rank-deficient and the system under-actuated. In this scenario, the MSCR is essentially in a constant state of internal singularity due to multiple axes of motion overlapping. Due to the aforementioned rank deficiency, a direct inverse matrix is undefined. While a pseudo-inverse can be computed, its application to an inverse kinematic approach results in an infinite set of suboptimal solutions. These solutions may not be viable due to actuation restrictions (current limits on the electromagnets employed) or unsuitable expected output shapes (Fig. 2).

Given that the catheter magnetization $\mathbf{m}$ (and therefore the magnetization to magnetic torque map $\mathbf{S}$) is fixed upon fabrication of the MSCR, we have reformulated the problem as one of linear optimization. Equation 6 may be rewritten as:

$$\begin{gathered} \underbrace{\mathbf{K}^{-1}\mathbf{J}^T\mathbf{S}}_{\mathbf{A}}\,\underbrace{\mathbf{B}_d}_{\mathbf{x}}\,\underbrace{=}_{=}\,\underbrace{\mathbf{Q}_d}_{\mathbf{b}} \\ \mathbf{x} \in \mathbb{R}^3 \text{ s.t. min } |\mathbf{Ax} - \mathbf{b}| \end{gathered} \tag{7}$$

with the $[.]_d$ subscript denominating desired quantities. This approach has been prototyped using the `lsqminnorm` function in the Matlab Optimization Toolbox and later implemented in C++.

B. Assumptions

Using Equation 7 as a starting point, a controller can be structured according to the following assumptions. These are put in place to both reduce the system's computational overhead and exploit the features of rigid-link assumptions for closed loop control:

1) While both the (deformed) magnetization to torque map $\mathbf{S}$ and the Jacobian matrix $\mathbf{J}$ are functions of the inputted set of desired angles $\mathbf{Q}$, they are assumed to be essentially constant during closed loop operation.
2) Inspection of Equation 6 reveals that, keeping all other terms constant, an increase in stiffness $\mathbf{K}$ would correspond to an equivalent increase in the magnitude of the resultant magnetic field $\mathbf{B}$ required. Recall that stiffness is a function of the material's assumed Young Modulus E (Equation 3) and the geometry of the catheter (both

of which are constant at run-time). We therefore assume that changes in $\mathbf{K}$ can me modeled for and compensated by changes in $\mathbf{B}$.

3) As a result of Assumptions 1 and 2, Equation 7 is reduced to a combination of constant terms, we can thus consider said expression as a linear map from a field to stacked deformation, $\mathbf{B}_t \mapsto \mathbf{Q}_t$ with the $[.]_t$ subscript denoting the quantities observed at time-step t.
4) In cases in which the magnetic field obtained from Equation 7 did not directly translate to the desired pseudo joint deflections $\mathbf{Q}_d$, it can be observed that the resulting deflection resembled the desired, but was lower in magnitude. This can be attributed to assumptions of linear, isotropic material behavior (Assumption 2) or other unmodeled external factors (such as gravity). It is assumed in these cases that the magnitude of the magnetic field obtained can be multiplied by a gain k to reduce global error.

C. Controller and Error

Following the assumptions laid out above, a controller was designed. While conventional controllers are developed to reject external disturbance, the aim here is to compensate for internal disturbances stemming from uncertainties in modeling assumptions, as well as external uncertainties related to the environment and the operating conditions.

Thus, it is first necessary to establish an error function and hence a method to quantify the difference between the observed and desired state of the MSCR. In this study, only planar behaviours are considered. As such, the error function can be reduced to an $n \times 1$ array with n representing the number of pseudo rigid-links. This is further reduced to a single scalar value via Equation 8. We can infer from Assumption 4 that the error observed in this problem must also be bound to a single dimension as a higher-dimensional error space would indicate a discrepancy in both the magnitude and direction of the applied field $\mathbf{B}_d$. In such an extreme scenario the simplifying assumptions in this control model would invalidate any solution as discussed in Section VI.

Embedded fibre reinforcements in the MSCR (as introduced in [25]), provide torsional resistance to the robot. This eliminates any out-of-plane deformation thus maintaining the error function bound to a single dimension. Having confirmed the dimensionality of the error function for planar control, a concrete metric can be established. Through the usage of a path-planning algorithm detailed in Section IV-D, a set of desired pseudo joint angles $\mathbf{q}_{\mathbf{d}_i}$ can be calculated and compared in real time with the observed pseudo joint angles $\mathbf{q}_{\mathbf{o}_i}$ present in the workspace. The average weighted error $\mathbf{e}$ is then given by:

$$\mathbf{e}(t) = \frac{\Sigma_{i=0}^{n}[(\mathbf{q_o}_i - \mathbf{q_d}_i)(i+1)]}{n} \tag{8}$$

As a result, we formulate a feedback control loop. Fig. 3 shows the developed control strategy, incorporating an adaption mechanism. This works on the basis established in Assumption 4, either directly altering the magnetic field

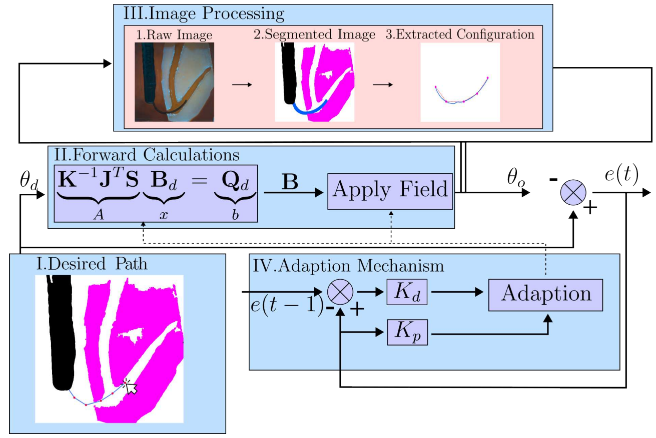

Fig. 3. Model-based closed loop implementation derived from Section III in diagram form and subdivided into 4 Steps. Step **I** provides desired angular deflections through path planning. Step **II** utilizes the expressions previously derived in Section II to obtain an initial solution, which is then applied to the real world. The output of this operation is observed in Step **III** where the acquired image is processed and thresholding applied to isolate the MSCR. From here the center-line is extracted via thinning. Angular deflections are fed back to the system to evaluate the error. In Step **IV** the error is utilized as an input to the *adaption* block, which determines whether the current state of the MSCR requires a large adjustment (adjust assumed stiffness and recompute the actuating field) or a minor field adjustment.

found solving Equation 7 or adjusting the assumed stiffness of the catheter, which will in turn restart the control loop by calculating a new solution.

IV. EXPERIMENTAL SETUP

A. Fabrication

The catheter fabrication process outlined in [25] is employed here. A nylon braid of external diameter 1 mm (Everlasto - James Lever 1856 Ltd, Manchester, U.K.) is held in axial alignment within a 1.8 mm internal diameter 50 mm length perspex tube using 3D printed end-caps. Mold cavities were filled with a mixture of Ecoflex-0030 (Smooth-On Inc, USA) and Neodymium-Iron-Boron (NdFeB) microparticles with an average diameter of 5 µm (MQFP-B+, Magnequench GmbH, Germany) in a mass ratio of 1:1. This composite was mixed and degassed in a high vacuum mixer (ARV-310, THINKYMIXER, Japan) at 1400 rpm, 20.0 kPa for 90 seconds. The mixture was injected into the tubing/molds and cured at room temperature for four hours. As previously reported in [25], the employed nylon braid increases the twisting stiffness of the catheter 20 times more than the increase in bending stiffness resulting in an effective bending modulus of the catheter of 500 KPa and twisting modulus of 10 MPa. Upon removal from the mold, the specimens were secured into a 3D printed magnetizing tray before being magnetized using an impulse magnetic field of 4.644 T (ASC IM-10-30, ASC Scientific, USA). Prior to the experiments being carried out, two (one per lumen present in the soft phantom as shown in Fig 5) referential set of desired configurations were calculated using the method detailed in Section IV-D. These configurations were utilized to calculate two separate magnetization directions that were then imparted onto the produced specimen.

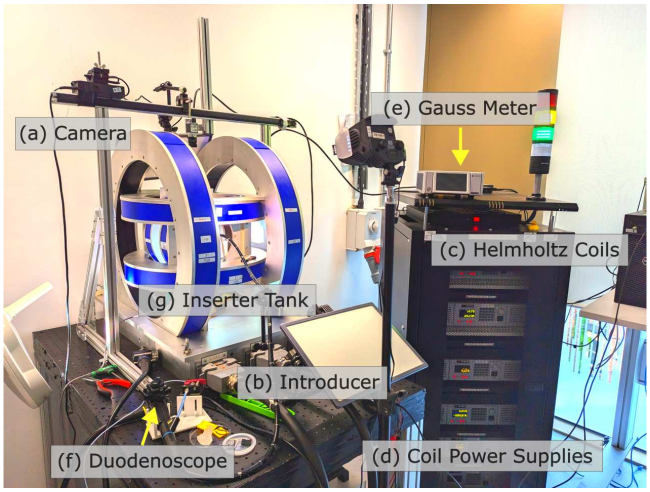

Fig. 4. The 3D Helmholtz Coil with camera setup for top-down view.

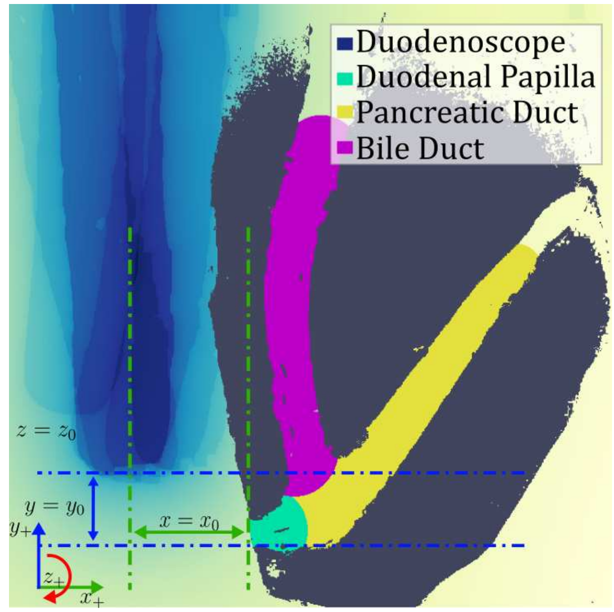

Fig. 5. The studied duodenoscope configurations are parametrized in the xy plane, with positive rotation clockwise about z. These parameters are used to identify each duodenoscope configuration studied. All configurations which permitted successful navigation into the phantoms' pancreatic duct (Table II) are superimposed in the background. The segmented soft phantom is also presented here for clarity.

B. Apparatus

Magnetic fields were generated utilizing a 3-D Helmholtz coil system (3DXHC12.5-300, Dexing Magnet Tech. Co., Ltd, Xiamen, China), which provided up to 25 mT in 3 orthogonal directions. Each individual coil is paired with a bipolar DC power supply (DXKDP, Dexing Magnet Tech. Co., Ltd, Xiamen, China), which are in turn controlled from a remote computer via the RS232 protocol. Similarly, a Nema 17 Stepper Motor (Micromech, U.K.) is managed by a UStepper S (http://ustepper.com) and in turn also remotely controlled, allowing to insert and retract a PTFE filament through a Duodenoscope (TJF-Q190V, Olympus Corporation, Japan) with an MSCR attached at the distal end. Image acquisition was carried out through Basler Ace camera (AC2040-120UC Basler AG, Ahrensburg, Germany) with a Basler C23-3518-5M-P f35 mm lens. The complete setup is pictured in Fig. 4. Experiments were carried out using a soft Ecoflex-Gel (Smooth-On Inc, USA) phantom representing the major papilla and its branching paths to the bile and pancreatic duct respectively. The phantom was submerged in a water died with a contrast agent to aid the image processing pipeline detailed in Section IV-C.

C. Image Processing

While the work presented here utilizes visual sensing for closed loop control, any clinical application would need to employ sensing techniques more suitable to the operating room, such as fluoroscopy or Fiber-Bragg Gratings. Thus, the image processing employed here was purposefully kept concise such that re-purposing for other sensing techniques can be easily achieved in later iterations.

Raw images were captured (Fig. 3(III.1)) and preliminary adjustments were made to remove glare and enhance contrast. A combination of thresholding, contour finding and smoothing were applied to isolate the soft phantom and duodenoscope Fig. 3(III.2)). These two isolated images are used to construct a cost-map that is used by the path planner described in Section IV-D. Using a similar procedure the MSCR is segmented from each frame it is present in. From here, $n + 1$ equally spaced link-length points along the center-line were found and treated as the pseudo joints interconnecting n pseudo rigid-links 3(III.3)).

D. Navigation

Using the cost-map calculated in Section IV-C, a standard implementation of the Theta* [26] path planning algorithm is used to calculate a path to a user defined goal. The outputted path is discretized into a set of pseudo rigid-links and used to calculate the initial magnetic field $\mathbf{B}_d$ for each insertion step. The MSCR is then inserted and the number of pseudo rigid-links present is inferred from the length of its centre-line and a known conversion factor between metric and image units. As previously detailed in III-C, the observed and desired configuration are then compared to produce an error, which is minimised by the controller. Due to the underactuated nature of the system, the error can only be minimised and not completely eradicated. Therefore, when a minimum is reached (the rate of change of the error reaches a stationary minimum), if the measured error is within tolerance, the control step is deemed successful. Following the successful completion of one link, the introducer resumed advancement, repeating the procedure iteratively until all links had been successfully inserted. At this point, the system similarly retracts the MSCR.

V. RESULTS

Using the controls mounted on the duodenoscope, the insertion position and angle can be altered. This procedure is typically carried out by a trained user utilizing a combination of an endoscopic camera mounted on the instrument as well

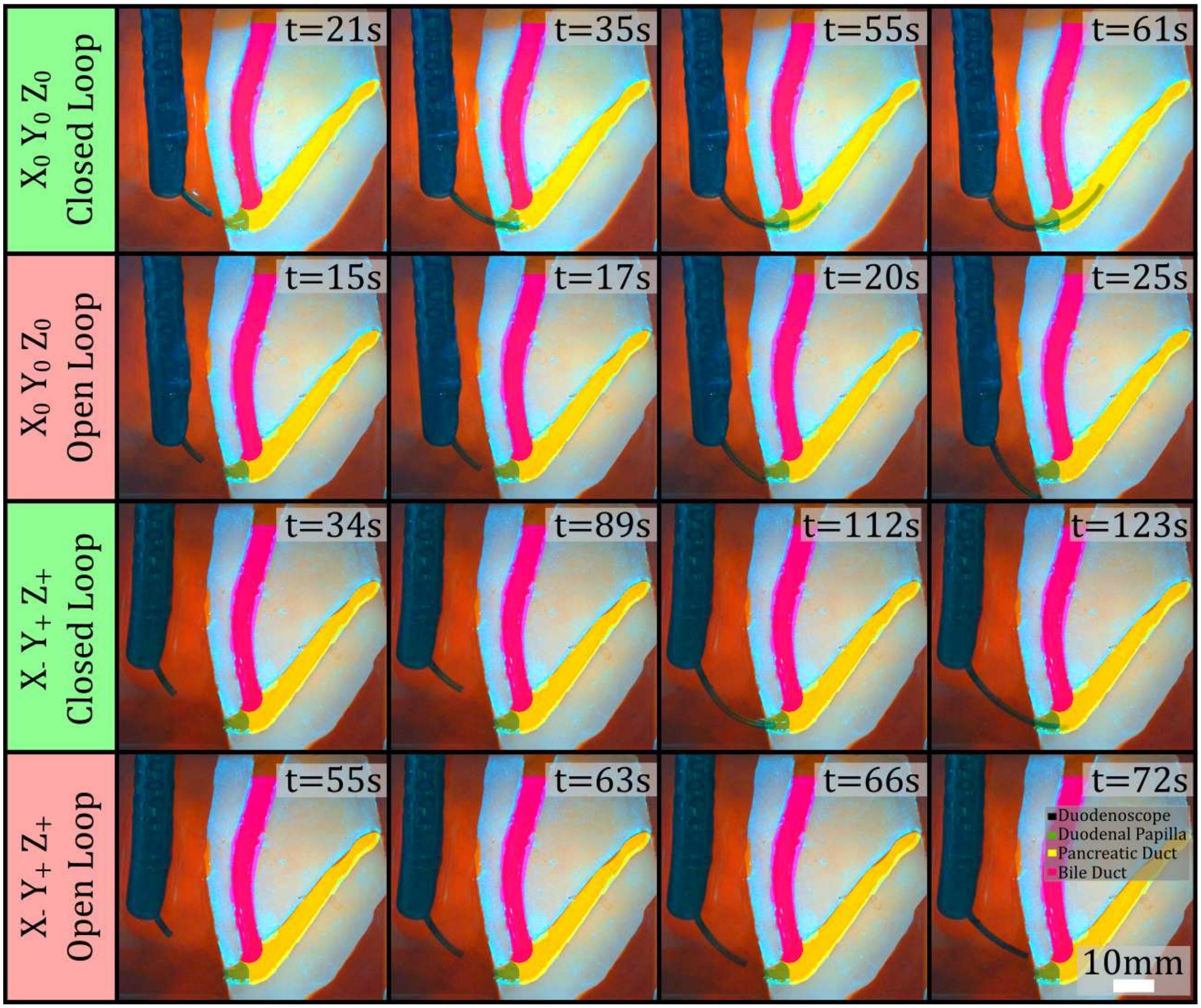

Fig. 6. Stills from a selection of the experiments presented in the supporting video, comparing closed and open loop performance while varying the duodenoscope configuration (as detailed in in Section IV-D, Fig. 5) and utilizing the same MSCR. Two pairs of open-loop and closed-loop experiments (x_0, y_0, z_0 and $x_-, y+, z+$) are provided with relevant timestamps. In both cases, the closed-loop iteration reaches the major duodenal papilla and navigates to the designated goal, while the open-loop iteration fails to enter through the papilla.

TABLE I
COMPARISON TABLE OF THE RESULTS REPORTED IN [5], [7], [13] AGAINST THOSE PRESENTED IN THIS LETTER.

	[7]	[5]	[13]	This Work
$\max\lvert\mathbf{B}\rvert$	50 mT	80 mT	Not disclosed	22 mT
Magnetization Profile	Continuous Magnetisation. Axial	Continuous Magnetisation. Axial	Oppositely Axially Magnetised Discrete Segments. Inert body	Continuous Magnetisation. Bespoke.
Control Methodology	Open Loop Tip Control	None	Closed Loop Tip Position and Orientation	Closed Loop Shape-forming
Reported Error	Tip Position Only: 0.5 mm	None	Tip Position and Orientation: 1.3 mm, 2.8°	Final Tip Position Error: 1.52 mm
Mean Weighted Shape Error	None	None	None	1.78mm CL 4.26mm OL

as some external imaging system, typically fluoroscopy. After selecting an arbitrary but navigable configuration as reference (Fig. 5), the inserting conditions are altered and parameterized following the convention detailed in Fig. 5. Fig. 6 shows stills taken from a selection of experiments featuring different duodenoscope configurations. Here, two pairs of closed-loop and open-loop experiments are shown for the x_0, y_0, z_0 and x_-, y_+, z_+ configurations. The closed-loop experiments both succeed in reaching the major duodenal papilla and then the user selected goal, while the open-loop trials (which employ

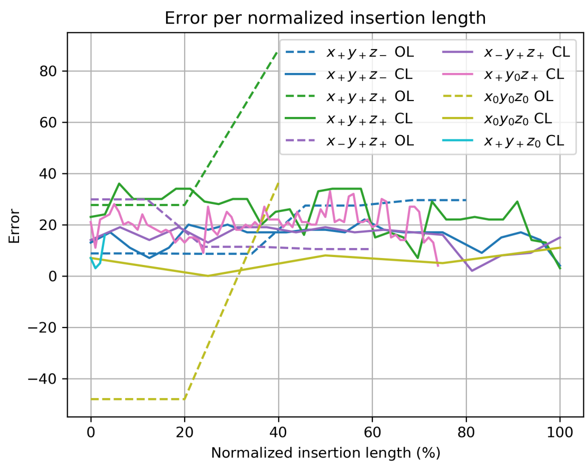

Fig. 7. Comparison of the recorded error during closed-loop and open-loop experiments. Errors were calculated using Equation 8. The open-loop errors are represented with dashed lines, with the closed-loop errors presented with solid lines. The error is normalized about the inserted length of MSCR in the given experiment. The average error recorded in all closed-loop experiments is 19%, while the average recorded error in all open-loop experiments is 25%.

TABLE II
SUMMARY OF THE DUODENOSCOPE CONFIGURATIONS STUDIED. THE PARAMETERIZATION IS DETAILED IN SECTION IV-B AND SHOWN IN FIG. 5.

Configuration			Closed Loop	Open Loop
x	y	z		
x_0	y_0	z_0	✓	×
x_-	y_+	z_+	✓	×
x_+	y_0	z_+	✓	×
x_+	y_+	z_-	✓	✓
x_+	y_+	z_+	✓	×

steps I, II only from Fig. 3) fail to reach the papilla. A full showcase of the configurations tested is presented in the supporting video, as well as in Table II. Additionally, all duodenoscope configurations that resulted in a successful navigation of the pancreatic duct are superimposed in Fig. 5.

While the principle focus of this letter is expanding the permissible poses of the scope from which successful navigations of the highly delicate pancreatic duct can be achieved, navigation of the bile duct is also shown for completeness in the supporting video. This also demonstrates some degree of generalizability of the solution.

VI. DISCUSSION AND FURTHER WORK

By employing bespoke magnetization profiles, an MSCR can be specifically designed to tackle a given morphology in space such as entering the pancreatic duct through the major papilla. A closed-loop shape control strategy has been devised to allow for multiple insertion positions and orientations not included in the catheter design to still result in successful navigation. Further, this semi-automated insertion and ability to choose a target location could assist a trained user to reach a specific part of the lumen to perform some functional task (drug release or to utilize a tool embedded within the MSCR).

To evaluate the impact of the proposed controller the range of configurations that can result in successful navigations under closed loop were also tested in open loop. In the majority of the configurations considered (Table II), the open loop approach failed to reach the papilla and hence navigate the duct, with a single known exception, as shown in the supporting video and Table II due to the favourable position and angle of insertion with respect to the soft phantom. Given the positioning and orientation of the duodenoscope would be determined by the user, employing the proposed control approach would result in a larger range of viable arrangements (Fig. 5), critically reducing the precision required from the user in placing the duodenoscope prior to navigation.

Further, the error recorded and calculated through Equation 8 is presented in graph form in Fig. 7. Here, the open-loop experiments are shown to conclude before a full insertion is achieved. Additionally, the average error in open-loop experiments (25%) is greater than that of closed-loop experiments (19%). Table I shows a brief comparison of the contributions presented in this letter and other similar works in the literature ([5], [7], [13]). While the proposed controller is not concerned only with the tip-position at any point, its final tip-placement error is comparable to that presented in [13]. The added complexities of shape forming control, however, prevent the controller from reaching the accuracies reported in [7]. Notably, the shape error (calculated with the same mechanism used in Equation 8) is only marginally greater than the final tip-only position error, while also maintaining minimal contact with the soft phantom walls and hence reducing contact forces. Further, the maximum magnetic field magnitude employed here is lower than that reported in the compared works.

The rigid-link framework developed as the foundation of the controller proposed here has been designed to accommodate both an n-link scenario and 3D shapes. However, the error metric utilized to guide the control process, as detailed in Section III-B, is bound to a single dimension. Therefore, adapting this controller to handle multi-dimensional error inputs in real time would necessitate adjustments. Additionally, the sensing technique currently employed will need to be extended for clinically relevant vision free environments, either by incorporating 3D external sensing, such as a C-arm, or by adopting embedded sensing, such as using Fiber Bragg Gratings [8]. Furthermore, the work developed above relies solely on homogeneous magnetic fields to generate wrenches and actuate the MSCR. Accounting for the major challenge that these under-actuated systems represent, future works pursuing shape-forming control would benefit from incorporating in-homogeneous magnetic fields (gradients) and their associated forces in any actuation strategy. The theoretical work presented here is already equipped for such an expansion, only needing to include magnetic gradients in the dipole to wrench mapping (Equation 5) and expand the actuation matrix $\mathbf{B} \in \mathbb{R}^3$ to $\mathbf{U} \in \mathbb{R}^8$, as has previously been reported in [22]. These added degrees of actuation would allow for more complex control of the MSCR and hence more elaborate possible MSCR shapes. Similarly tied to the implementation of the controller, the initial solution found in Section III-A is obtained by utilizing a least-mean-norm solution. Whilst this kind of solving method provides an accurate response with reasonably low computational overheads, it comes with the caveat of underfitting the found solution in the case of inputs being strongly present in both negative and positive quadrants (notably, generating "S" shaped curves). Thus, further developments would utilize a different real-time solution method that may be able to account for composite shapes, such as gradient descent [13].

ACKNOWLEDGEMENT

The authors would like to thank Samwise Wilson for the technical assistance in developing the experimental arrangements used in this work.

REFERENCES

[1] P. Dupont, N. Simaan, H. Choset, and C. Rucker, "Continuum Robots for Medical Interventions," *Proceedings of the IEEE*, pp. 1–24, 2022. [Online]. Available: https://ieeexplore.ieee.org/document/9707607/

[2] D. Shimizu, T. Yamano, Y. Kudo, M. Kuroda, S. Takagi, E. Ikeda, M. Kenmotsu, and H. Tsuji, "Diagnostic and therapeutic role of endoscopic retrograde pancreatography and stent placement for grade IV blunt pancreatic trauma: A case report," *Trauma Case Reports*, vol. 28, p. 100319, Aug. 2020. [Online]. Available: https://www.sciencedirect.com/science/article/pii/S2352644020300431

[3] O. Strobel, J. Neoptolemos, D. Jäger, and M. W. Büchler, "Optimizing the outcomes of pancreatic cancer surgery," *Nature Reviews Clinical Oncology*, vol. 16, no. 1, pp. 11–26, Jan. 2019. [Online]. Available: https://www.nature.com/articles/s41571-018-0112-1

[4] T. d. Veiga, J. H. Chandler, P. Lloyd, G. Pittiglio, N. J. Wilkinson, A. K. Hoshiar, R. A. Harris, and P. Valdastri, "Challenges of continuum robots in clinical context: a review," *Progress in Biomedical Engineering*, vol. 2, no. 3, p. 032003, Jul. 2020, publisher: IOP Publishing. [Online]. Available: https://dx.doi.org/10.1088/2516-1091/ab9f41

[5] Y. Kim, G. A. Parada, S. Liu, and X. Zhao, "Ferromagnetic soft continuum robots," *Science Robotics*, vol. 4, no. 33, p. eaax7329, Aug. 2019, publisher: American Association for the Advancement of Science. [Online]. Available: https://www.science.org/doi/10.1126/scirobotics.aax7329

[6] J. Edelmann, A. J. Petruska, and B. J. Nelson, "Magnetic control of continuum devices," *The International Journal of Robotics Research*, vol. 36, no. 1, pp. 68–85, Jan. 2017, publisher: SAGE Publications Ltd STM. [Online]. Available: https://doi.org/10.1177/0278364916683443

[7] Y. Ni, Y. Sun, H. Zhang, X. Li, S. Zhang, and M. Li, "Data-Driven Navigation of Ferromagnetic Soft Continuum Robots Based on Machine Learning," *Advanced Intelligent Systems*, vol. 5, no. 2, p. 2200167, 2023. [Online]. Available: https://onlinelibrary.wiley.com/doi/abs/10.1002/aisy.202200167

[8] G. Pittiglio, J. H. Chandler, T. da Veiga, Z. Koszowska, M. Brockdorff, P. Lloyd, K. L. Barry, R. A. Harris, J. McLaughlan, C. Pompili, and P. Valdastri, "Personalized magnetic tentacles for targeted photothermal cancer therapy in peripheral lungs," *Communications Engineering*, vol. 2, no. 1, pp. 1–13, Jul. 2023, number: 1 Publisher: Nature Publishing Group. [Online]. Available: https://www.nature.com/articles/s44172-023-00098-9

[9] D. Lin, N. Jiao, Z. Wang, and L. Liu, "A Magnetic Continuum Robot with Multi-Mode Control Using Opposite-Magnetized Magnets," *IEEE Robotics and Automation Letters*, vol. 6, no. 2, pp. 2485–2492, Apr. 2021, publisher: Institute of Electrical and Electronics Engineers Inc.

[10] F. Xu, H. Wang, W. Chen, and Y. Miao, "Visual Servoing of a Cable-Driven Soft Robot Manipulator with Shape Feature," *IEEE Robotics and Automation Letters*, vol. 6, no. 3, pp. 4281–4288, Jul. 2021, publisher: Institute of Electrical and Electronics Engineers Inc.

[11] R. Ahmed, M. Ilami, J. Bant, B. Beigzadeh, and H. Marvi, "A Shapeshifting Ferrofluidic Robot," *Soft Robotics*, vol. 8, no. 6, pp. 687–698, Dec. 2021, publisher: Mary Ann Liebert, Inc., publishers. [Online]. Available: https://www.liebertpub.com/doi/full/10.1089/soro.2019.0184

[12] J. Sikorski, A. Denasi, G. Bucchi, S. Scheggi, and S. Misra, "Vision-Based 3-D Control of Magnetically Actuated Catheter Using BigMag—An Array of Mobile Electromagnetic Coils," *IEEE/ASME Transactions on Mechatronics*, vol. 24, no. 2, pp. 505–516, Apr. 2019, conference Name: IEEE/ASME Transactions on Mechatronics.

[13] D. Lin, W. Chen, K. He, N. Jiao, Z. Wang, and L. Liu, "Position and Orientation Control of Multisection Magnetic Soft Microcatheters," *IEEE/ASME Transactions on Mechatronics*, pp. 1–12, 2022, conference Name: IEEE/ASME Transactions on Mechatronics.

[14] V. K. Venkiteswaran, J. Sikorski, and S. Misra, "Shape and contact force estimation of continuum manipulators using pseudo rigid body models," *Mechanism and Machine Theory*, vol. 139, pp. 34–45, Sep. 2019. [Online]. Available: https://www.sciencedirect.com/science/article/pii/S0094114X18318706

[15] N. Murasovs, V. Francescon, P. Lloyd, M. D. Lecce, D. S. Chathuranga, G. Pittiglio, O. Onaizah, J. H. Chandler, and P. Valdastri, "Breathing Compensation in Magnetic Robotic Bronchoscopy via Shape Forming," *IEEE Robotics and Automation Letters*, vol. 9, no. 10, pp. 9055–9062, Oct. 2024, conference Name: IEEE Robotics and Automation Letters. [Online]. Available: https://ieeexplore.ieee.org/document/10592800/?arnumber=10592800

[16] T. Da Veiga, J. H. Chandler, G. Pittiglio, P. Lloyd, M. Holdar, O. Onaizah, A. Alazmani, and P. Valdastri, "Material Characterization for Magnetic Soft Robots," in *2021 IEEE 4th International Conference on Soft Robotics (RoboSoft)*. New Haven, CT, USA: IEEE, Apr. 2021, pp. 335–342. [Online]. Available: https://ieeexplore.ieee.org/document/9479189/

[17] K. A. Khan, P. Nardelli, A. Jaeger, C. O'Shea, P. Cantillon-Murphy, and M. P. Kennedy, "Navigational Bronchoscopy for Early Lung Cancer: A Road to Therapy," *Advances in Therapy*, vol. 33, no. 4, pp. 580–596, Apr. 2016. [Online]. Available: http://link.springer.com/10.1007/s12325-016-0319-4

[18] W. Waddingham, U. Kamran, B. Kumar, N. J. Trudgill, Z. P. Tsiamoulos, and M. Banks, "Complications of diagnostic upper Gastrointestinal endoscopy: common and rare – recognition, assessment and management," *BMJ Open Gastroenterology*, vol. 9, no. 1, p. e000688, Dec. 2022, publisher: BMJ Specialist Journals Section: Endoscopy. [Online]. Available: https://bmjopengastro.bmj.com/content/9/1/e000688

[19] G. Pittiglio, P. Lloyd, T. da Veiga, O. Onaizah, C. Pompili, J. H. Chandler, and P. Valdastri, "Patient-Specific Magnetic Catheters for Atraumatic Autonomous Endoscopy," *Soft Robotics*, vol. 9, no. 6, pp. 1120–1133, Dec. 2022, publisher: Mary Ann Liebert, Inc., publishers. [Online]. Available: https://www.liebertpub.com/doi/10.1089/soro.2021.0090

[20] J. J. Abbott, E. Diller, and A. J. Petruska, "Magnetic Methods in Robotics," *Robotics, and Autonomous Systems Annu. Rev. Control Robot. Auton. Syst. 2020*, vol. 13, pp. 57–90, 2020. [Online]. Available: https://doi.org/10.1146/annurev-control-081219-

[21] R. J. Webster and B. A. Jones, "Design and Kinematic Modeling of Constant Curvature Continuum Robots: A Review," *The International Journal of Robotics Research*, vol. 29, no. 13, pp. 1661–1683, Nov. 2010, publisher: SAGE Publications Ltd STM. [Online]. Available: https://doi.org/10.1177/0278364910368147

[22] S. Salmanipour and E. Diller, "Eight-degrees-of-freedom remote actuation of small magnetic mechanisms," in *Proceedings - IEEE International Conference on Robotics and Automation*. Institute of Electrical and Electronics Engineers Inc., Sep. 2018, pp. 3608–3613, iSSN: 10504729.

[23] Y. Kim and X. Zhao, "Magnetic Soft Materials and Robots," *Chemical Reviews*, p. acs.chemrev.1c00481, Feb. 2022. [Online]. Available: https://pubs.acs.org/doi/10.1021/acs.chemrev.1c00481

[24] Q. Boehler, S. Gervasoni, S. L. Charreyron, C. Chautems, and B. J. Nelson, "On the Workspace of Electromagnetic Navigation Systems," *IEEE Transactions on Robotics*, pp. 1–17, 2022. [Online]. Available: https://ieeexplore.ieee.org/document/9868240/

[25] P. Lloyd, O. Onaizah, G. Pittiglio, D. K. Vithanage, J. H. Chandler, and P. Valdastri, "Magnetic Soft Continuum Robots With Braided Reinforcement," *IEEE Robotics and Automation Letters*, pp. 1–8, 2022. [Online]. Available: https://ieeexplore.ieee.org/document/9832475/

[26] R. Rey, "robotics-upo/Heuristic_path_planners," Jul. 2024, original-date: 2021-05-17T07:50:38Z. [Online]. Available: https://github.com/robotics-upo/Heuristic_path_planners